AIAA SciTech Forum
8-12 January 2024, Orlando, FL
AIAA SCITECH 2024 Forum

10.2514/6.2024-1546

Plasma Discharge Variance and Beamlet Trajectories of Alternative Propellants in ECR Gridded Ion Thruster

Joshua R. Tompkins[1], Richeek Dutta[2], and Joshua L. Rovey[3]
University of Illinois at Urbana-Champaign, Urbana, IL, 61801, United States

Evaluation of alternatives to traditional xenon propellant has become an increasingly important area of study for electric space propulsion. Myriad thruster configurations and ionization schemes have been considered with electron cyclotron resonance offering great potential due to its relative insensitivity to reactive atomic species such as oxygen. This study borrows from the design methodology of a 10-cm-class waveguide ECR gridded ion thruster as a test bed for alternative propellants. The thruster design process, simulation of magnetic and electric fields inside the waveguide and plasma discharge chamber are presented. Experimental evaluation of the downstream plasma properties are reported for argon, nitrogen, and air propellants at mass flowrates of 75, 100, 150, and 200 µg/s and absorbed microwave power ranging from approximately 5 to 20 W. The argon propellant saw a range of electron temperatures from 1.4 to 2.3 eV with corresponding number densities of $8.1\text{x}10^{13}$ to $2.8\text{x}10^{14}$ m^{-3}. Similar electron temperature ranges for nitrogen and air observed were 2.1 to 4.1 eV and 1.8 to 3.4 eV, respectively. Number density ranges of $1.04\text{x}10^{13}$ to $2.4\text{x}10^{14}$ m^{-3} for nitrogen, and $6.0\text{x}10^{13}$ to $1.6\text{x}10^{14}$ m^{-3} for air are reported. Spatial variation of the plasma discharge is considered on the basis of propellant species, absorbed power, mass flowrate, and angle relative to the monopole antenna. Emitted light intensity distributions are compared with the magnetic field geometry inside the discharge chamber to elucidate the observed asymmetry. Additionally, ion trajectory modeling is undertaken using SIMION with development of the code presented with qualitative comparison to literature. A grid geometry case study is performed and results for xenon, argon, N_2, and O_2 are presented.

I. Introduction

Within the last decade, the realm of electric space propulsion has seen a greater push towards investigating and implementing thruster systems that operate using non-traditional propellants with water vapor being particularly of interest [1–5]. The appeal of such systems has become more broadly apparent given the increasing price and rarity of Xenon and Krypton gases. Traditional gridded ion thrusters utilizing a cathode for ionization are restricted in terms of possible alternative propellants based on the operating limitations of the cathode material [5]. Plasma generation through microwave electron cyclotron resonance (ECR) offers a means to overcome material limitations by removing the cathode requirement altogether. Moreover, microwave ECR plasma thrusters have been successfully implemented using both traditional and alternative propellants in magnetic nozzle and gridded ion configurations [3,6–10]. An ECR gridded ion thruster, µ10, was successfully implemented by JAXA in the Hayabusa 1 and 2 missions producing ion beam currents of 130 mA and 178 mA, respectfully. This design has been further refined to improve ion beam current extraction to 207 mA for xenon propellant [11]. Further evaluation of the µ10 thruster system in configurations matching the Hayabusa2 and DESTINY+ missions has demonstrated the ability to achieve thrust outputs with krypton comparable to that of xenon [7,8]. The principal drawback of operating with krypton in this manner was the 30 % reduction in the overall performance of the thruster, which the authors attributed to the need for higher neutralizer mass flow. The appeal of krypton has led to exploration of use and comparison with xenon, typically within the context of ECR magnetic nozzles [10,12] or gridded ion configurations [7,8,13] with some focus on helicon discharge of krypton in a magnetic nozzle [14].

[1] Graduate Research Assistant, Department of Aerospace Engineering.
[2] Undergraduate Research Assistant, Department of Aerospace Engineering.
[3] Professor, Department of Aerospace Engineering, and AIAA Associate Fellow.

While krypton is an attractive substitute to xenon there has also been considerable focus on the investigation of water vapor as an alternative propellant through computational, experimental, and systems level studies [1–3,9,15–18]. The departure from utilizing noble gas propellants introduces new loss mechanisms associated with molecular propellants in the form of dissociative ionization and excitation as well as rotational, vibrational and electronic excitation not present with monoatomic species [1,2,15,16]. The AQUAJET magnetic nozzle thruster has demonstrated a similar magnitude of thrust with water vapor producing 0.1-0.2 mN as compared to xenon at 0.3-0.4 mN for flowrates of 0.14 mg/s and 0.10-0.20 mg/s, respectively [9]. Of course, the tradeoff comes in the form of thruster efficiency decreases from 0.9-1.0 % for xenon to 0.1-0.2 % with water vapor. Similar performance estimates for water vapor have been reported within the context of an ECR gridded ion thruster with Akata et al. predicting a thrust output of 190 μN and a thruster efficiency of 1.0 % [17].

A key performance aspect of ECR plasma gridded ion thrusters is the relationship between propellant flowrate and screen/beam current [11,19–21]. In general, for a discharge chamber and ion optics configuration, there exists an optimal propellant flowrate whereby further increases do not improve beam current extraction. However, it has been shown in literature that in certain operational cases and configurations it is possible to inject the optimal propellant flowrate and extract considerably less beam current than the optimal output for the same flowrate [21]. This observation has been discussed as plasma hysteresis, and has been explored with Xenon, whereby the plasma discharge producing suboptimal beam current extraction is called “low-current” mode while the discharge providing greater beam current is called “high-current" mode by Yamashita et al. in 2021 [21]. Effectively, there exists some combination of operating conditions by which the extracted beam current drops markedly with increasing flowrate. This is irregular as under a similar flowrate it may be possible to extract more than twice the amount of ion beam current. Interestingly, this sudden reduction in beam current output seemingly correlates with a visible change in the light emission from the plasma discharge chamber (PDC), and in the case of the μ10 thruster, this reduction has been attributed to plasma formation inside the thruster waveguide. However, in the case of a 5 cm ECR gridded ion thruster with no waveguide operating with a planar antenna, a similar jump in ion beam current is observed. Fu and Ding in 2021 present a marked increase in ion beam current that correlates with a change in visual discharge appearance with increasing microwave power [22]. The authors consider this variability through comparison of light intensity across the grid face and present the change in the discharge with respect to the magnetic field and microwave propagation. The authors ultimately hypothesize that a shift from O-mode plasma generation to a combined O-mode and X-mode propagation drives the discharge region to spread radially outward, thereby increasing the ion beam current.

In order to investigate the use of alternative propellants, a 10-cm class ECR gridded ion thruster has been designed and fabricated at the University of Illinois at Urbana-Champaign. This thruster design draws inspiration from the μ10 implemented by JAXA and incorporates many of the improvements made throughout the years of development. The goal of this study is to experimentally investigate the ECR plasma discharge characteristics of argon and alternative propellants such as nitrogen and air. Of particular interest are the conditions by which the plasma discharge mode changes and how absorbed microwave power, propellant flowrate, and propellant species affect the discharge parameters. Will the high-current/low-current modes be present for molecular propellant species or is this specific to noble gases? Evaluation of the downstream plasma properties at varied operating parameters as well as consideration for spatial variance in the plasma are evaluated and compared to optical emissions inside the PDC. We show here that the high-current/low-current ECR modes identified for noble gases are also present for nitrogen, and correlate with visual optical emission changes in the internal discharge plasma structure. Further, we show here that the external grid-plane plasma properties and profiles are also correlated with the visual changes in the internal discharge plasma structure.

II. Experimental Methods

A. ECR Thruster Design

The thruster is a cathode-less design where waveguided microwaves provide energy to electrons in a permanent magnetic field through the process of electron cyclotron resonance (ECR). The relation of cyclotron frequency for electrons to incident electromagnetic waves is given in Equation 1.

$$\omega_c = 2\pi f_c = \frac{qB}{m_e} \tag{1}$$

where ω_c is the angular cyclotron frequency of electrons, f_c is the linear cyclotron frequency, q is the charge of a particle (in this case it is the elementary charge of an electron), B is the magnetic field strength at resonance, and m_e is the mass of an electron. From a design perspective, the incident microwave frequency is a chosen parameter while

electron mass and charge are fixed values assuming no relativistic effects. With our chosen incident frequency of 2.57 GHz, ECR heating will occur at a magnetic field strength of 91.8 mTesla (918 Gauss). To achieve such a high permanent magnetic field strength, samarium cobalt (SmCo) ring magnets are utilized inside the PDC, which terminates at one end of the waveguide. The design of the waveguide was considered based on the desire for sole resonance of the TE_{111} propagating mode. The waveguide's inner diameter was chosen to be 74 mm and its length was determined by Equation 2.

$$f_{r,111} = \frac{c}{2\pi}\sqrt{\frac{p'_{11}{}^2}{a} + \frac{\pi^2}{d}} \tag{2}$$

where $f_{r,111}$ is the resonant frequency of the TE_{111} mode, c is the speed of light in a vacuum, p'_{11} is the Extrema of the Bessel function corresponding to the TE_{11} mode, a is the radius of the cylindrical waveguide, and d is the length of the waveguide. The dimensions of the thruster were chosen based on the criteria specified so that the highest electric field intensity region would correspond spatially to the location of the ECR region inside the PDC.

B. ECR Thruster

Design of the PDC magnetic field was undertaken iteratively using ANSYS Maxwell. A 2D plot of the ECR field strength is presented in Fig. 1.

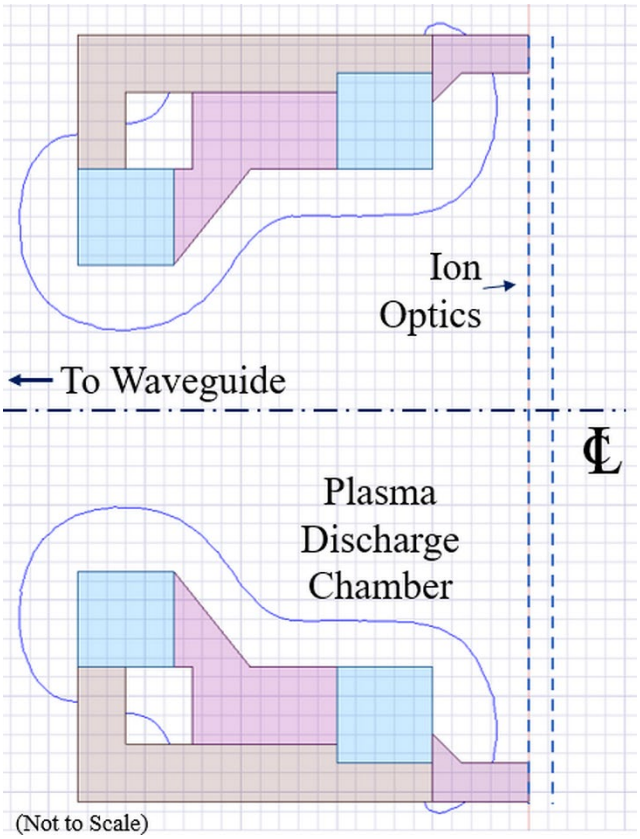

Fig. 1 Plasma Discharge Chamber ECR Magnetic Field Line (918 G).

The blue squares depicted in Fig. 1 represent the SmCo magnets, the magenta-colored bodies correspond to non-magnetic 316 stainless steel retention rings, and the brown L-shaped piece is a magnetic iron yoke. With the dimensions of the PDC determined by the iterative design approach, and the TE_{111} propagation mode defining the remaining dimensions of the waveguide, simulations of the electric field produced by the input microwaves was undertaken using ANSYS High-Frequency Structure Simulator (HFSS). The electric field intensity depicted in Fig. 2 is in the absence of a plasma and corresponds to propagation in vacuum. The higher intensity region of the electric field is favorably positioned within the area where the portion of the waveguide/PDC where the rear SmCo ring magnet is situated. The left portion of Fig. 3 denotes the locations of the two SmCo ring magnets, stainless steel retention

rings, iron yoke, and propellant manifold. All PDC components are inside an aluminum housing with an aluminum waveguide attached near the rear SmCo magnet. The ion optics employed were based on the optimal beam current extraction obtained by Yamashita et al. for Xenon propellant with the 108 mm beam diameter of the μ10 thruster [21]. The dimensions of the ion optics for this thruster are presented in Table 1, and the grids were made from photoetched molybdenum.

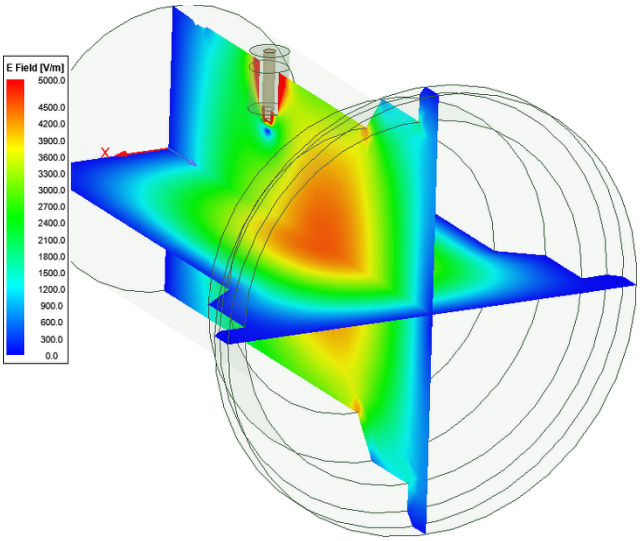

Fig. 2 ANSYS HFSS electric field simulation for 2.57 GHz and 10 W input power.

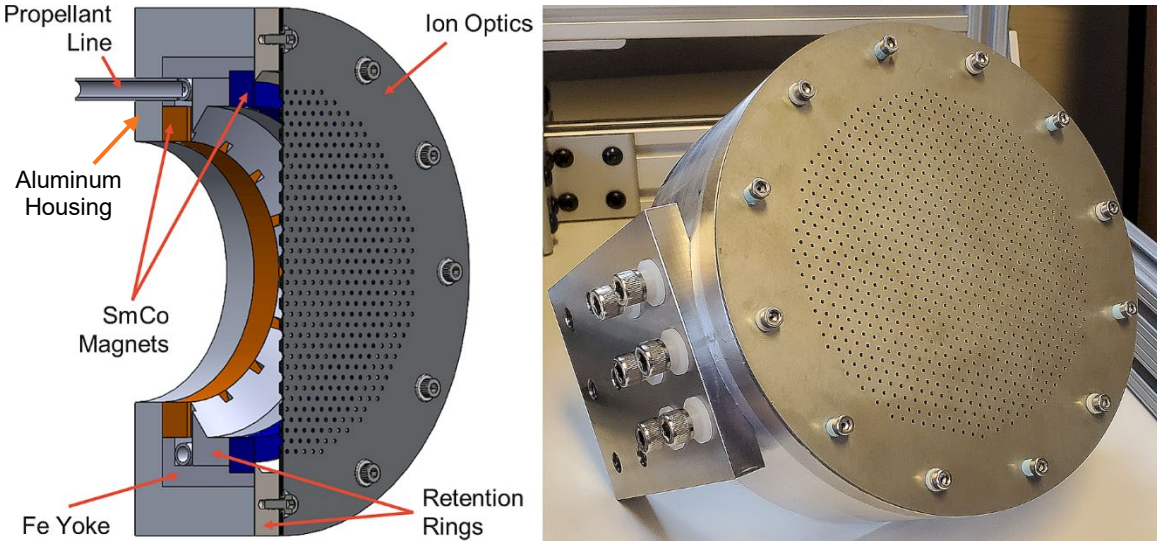

Fig. 3 Left: CAD model of PDC. Right: Assembled thruster without waveguide.

Table 1 Ion Optics Configuration

Grid	Screen	Accel
Thickness [mm]	0.5	0.5
Aperture Diameter [mm]	3.05	1.2
Aperture Count	855	855
Open Area [%]	68.2	10.56

C. Magnetic Field Mapping

The permanent magnetic field inside the PDC and a portion of the waveguide was mapped using a Senis 3MTS Teslameter. The Teslameter was mounted on a Newmark Systems NLS4 linear stage which traversed laterally across the inside diameter of thruster. These lateral measurements were conducted in 1 mm steps depth-wise starting approximately 1 mm from the interior face (plasma side) of the screen grid. Fig. 4 presents a contour plot of the experimentally mapped magnetic field inside the PDC with the ECR field strength of 91.8 mTesla depicted by the solid black line. Comparison of Fig. 1 and Fig. 4 presents disagreement in the continuity of the ECR field line throughout the PDC. Two-dimensional modelling of the magnetic field indicated the ECR field line would not intercept the thruster body walls, while the experimentally measured magnetic field does show the ECR field line intercepting the thruster body.

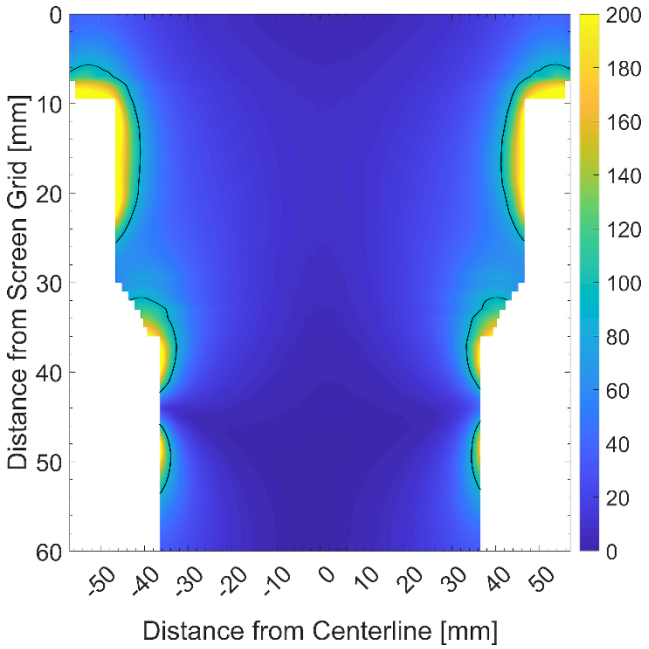

Fig. 4 Experimental mapping of magnetic field in PDC (black line denotes ECR field strength of 91.8 mTesla).

D. Vacuum Facilities

Experiments were conducted in a 1.2-m-diameter by 2.1-m-length vacuum chamber at the Electric Propulsion Laboratory at the University of Illinois Urbana-Champaign. Two Kinney KT150 piston pumps, a Roots 615 blower, and an NRC blower provide the initial 50×10^{-3} Torr vacuum needed before switching to a single TM1200 cryopump, which eventually provides a base background chamber pressure of approximately 3.4×10^{-8} Torr. The propellant flowrate was regulated by an Alicat mass flow controller model MCS-10SCCM-D-PCA10/5M, and the propellants utilized in this study were research grade Argon and Nitrogen as well as Ultra Zero grade air. The mass flow rates investigated in this study were 75, 100, 150, and 200 µg/s with the average background chamber pressure for each propellant at the four flowrates reported in Table 2. Fig. 5 provides a schematic of the vacuum facilities utilized as well as the electronics related to microwave ECR plasma generation and power monitoring.

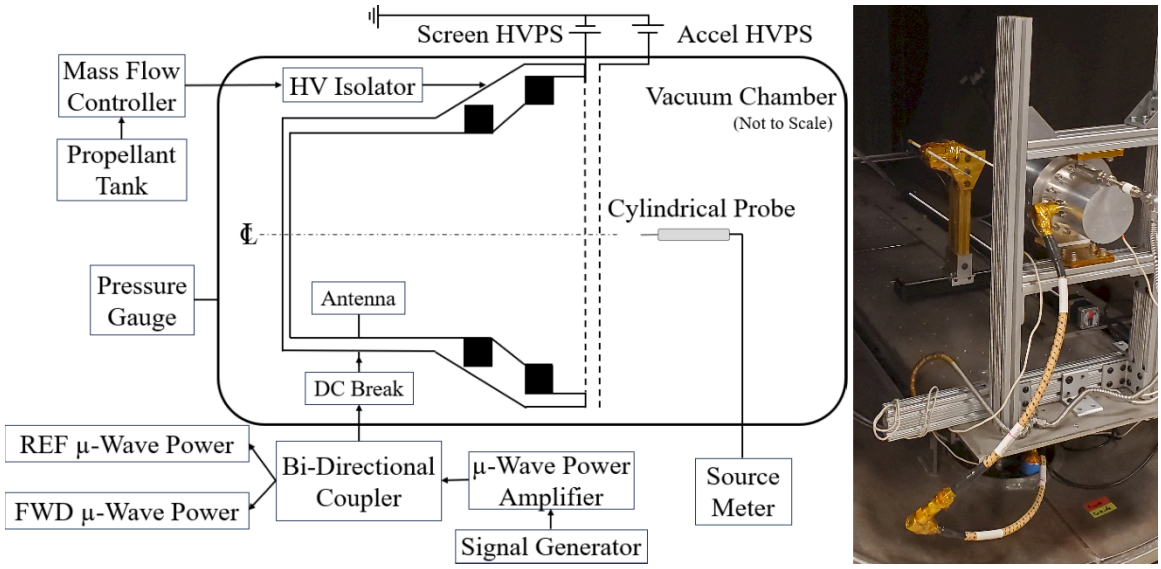

Fig. 5 Left: Schematic of vacuum facilities. Right: Experimental setup.

Table 2 Chamber Pressure at Testing Parameters [μTorr]

Flowrate	75 μg/s	100 μg/s	150 μg/s	200 μg/s
Argon	0.26	0.34	0.49	0.65
Nitrogen	0.37	0.46	0.63	0.83
Air	0.38	0.48	0.69	0.87

E. Plasma Diagnostics

Plasma properties were measured with a cylindrical Langmuir probe positioned 4 mm downstream from the exit plane of the acceleration grid. The probe was constructed by embedding a tungsten wire, with a diameter of 0.11 mm and an exposed length of 3.6 mm, inside hollow alumina rods with gaps filled by Ceramabond 569. The tungsten wire was electrically coupled to the center conductor of a shielded BNC cable which fed outside of the vacuum chamber to a Keithley 2410 SourceMeter. The SourceMeter was utilized to collect IV-traces at specific locations across the face of the ion optics with a Velmex XSlide linear motion stage controlling the position of the probe. The SourceMeter was controlled using a custom LabVIEW program which collected the probe current while sweeping the voltage from -50 V to +70 V in 0.2 V increments while averaging the current based on three measurements at each voltage step. A linear fit was applied for each IV-trace between -45 V and -30 V, subtracting the ion current contribution across the swept voltage range. The plasma potential was obtained through the inflection point method by plotting the numerical first derivative of the IV-trace while evaluation of the electron temperature was achieved based on the linear fitting method described by Li et al [23]. The transition region of the $\mathrm{Ln}|I_e|$ curve chosen was approximately centered around the floating potential observed with the plot of $\mathrm{Ln}|I|$. The left image in Fig. 6 provides an example of the inflection point method employed the right image presents a similar demonstration of the linear fitting approach for electron temperature. With the electron temperature known and finding the electron saturation current from the plasma potential, the calculation of electron number density was performed based on Equation 3 [23],

$$n_e = \frac{I_{e,sat}}{qA_p}\sqrt{\frac{2m_e}{\pi k_B T_e}} \tag{3}$$

where n_e is the electron number density in m^{-3}, A_p is the probe current collection area in m^2, k_B is the Boltzmann constant, and T_e is the electron temperature.

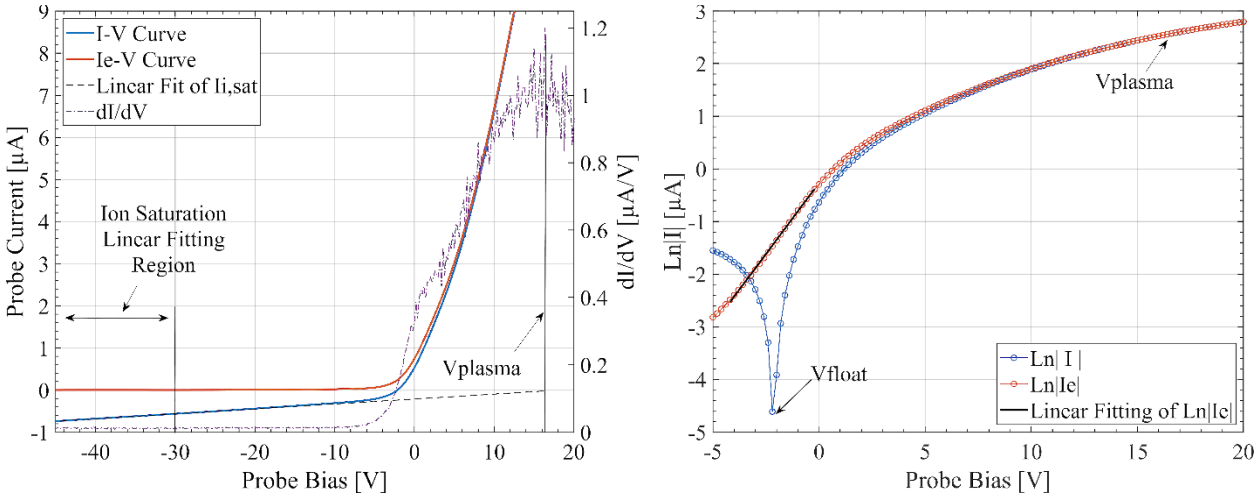

Fig. 6 Argon discharge at 100 µg/s, 2.57 GHz, and P_{abs} = 18.95 W. Left: Demonstration of inflection point method. Right: Demonstration of linear fitting method.

III. Experimental Results

A. Visual Plasma Appearance

1. General Trends

Visually, the discharge plasma has spatial variance dependent on the flowrate and propellant species. Fig. 7 shows the two main discharge rings of the plasma. The left image in Fig. 7 is a typical discharge at lower mass flowrates with the dominant plasma ring occurring at a larger radius. In contrast, the right image of Fig. 7 is typical for higher flowrates, wherein the dominant plasma discharge ring occurs at a smaller radius, closer to the thruster centerline. These images show variance in the location of the dominant plasma ring, but they also illustrate a mixed discharge between the two primary rings. Plasma is produced at both ring locations in both images, with changes in which plasma ring visually appears dominant. Additionally, the intensity of the light emitted from the plasma appears asymmetric with respect to the azimuthal direction. Consider the right image of Fig. 7, it is apparent that the light intensity in the top right corner or the outer ring is greater than the light intensity in the top left corner.

Fig. 8 clearly demonstrates how increasing flowrate leads to the observed shrinking of the primary discharge ring radius for an Argon discharge at all four flowrates investigated. The top row of Fig. 8 presents discharge for a mean P_{abs} of 5.72 W while the bottom row is for a mean P_{abs} of 19.35 W. From the visual appearance of the discharge images presented in Fig. 8 two trends are apparent: high power absorption results in a generally brighter discharge and that increasing the flowrate from 100 µg/s to 150 µg/s causes the aforementioned reduction in the discharge ring radius. This result is similar to the reported plasma hysteresis response observed by Yamashita et al. in 2021 with increasing Xenon mass flowrate [10]. The measured ion beam current would rapidly decrease with increasing flowrate with the specific value where this occurred dependent on the various combination of screen and acceleration optics employed. A potentially important distinction between that study and this one is the absence of beam extraction in our results. While the optics configuration and bias of the grids contribute to the discharge change as reported by Yamashita, these same trends are apparent without beam extraction, and it appears that mass flowrate is the greatest factor in contributing to this variance. Unfortunately, the lower flowrates investigated prohibited stable discharge for both the nitrogen and air propellant species at low P_{abs}. Consequently, a similar comparison as was made in Fig. 8 is not possible.

Fig. 9 presents the variation with flowrate for nitrogen and air cases for each flowrate at mean P_{abs} values of 19.52 W and 19.32 W, respectively, with σ values representing the standard deviation of P_{abs} between the four flowrates. In the case of nitrogen, we see a subtle shift in the discharge location away from the larger plasma ring towards the centerline with increasing flowrate. On the contrary, the air discharge remains relatively consistent in its discharge location with the brightest discharge ring occurring consistently at the larger radius. Although, for both nitrogen and air, the overall brightness of the discharge does not lend itself to ease of analysis.

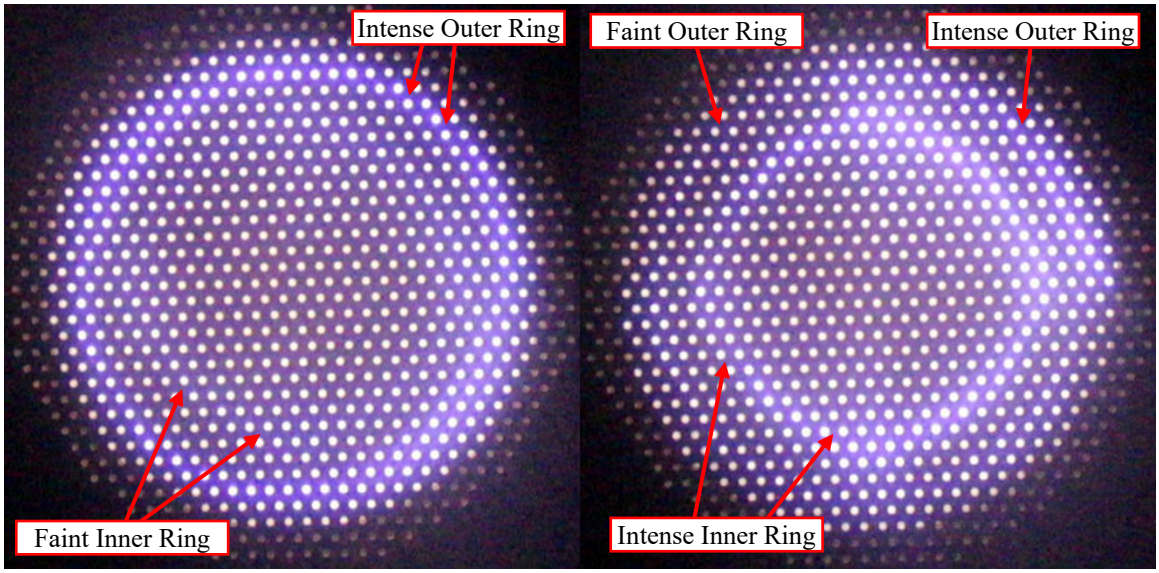

Fig. 7 Demonstration of plasma discharge variance.

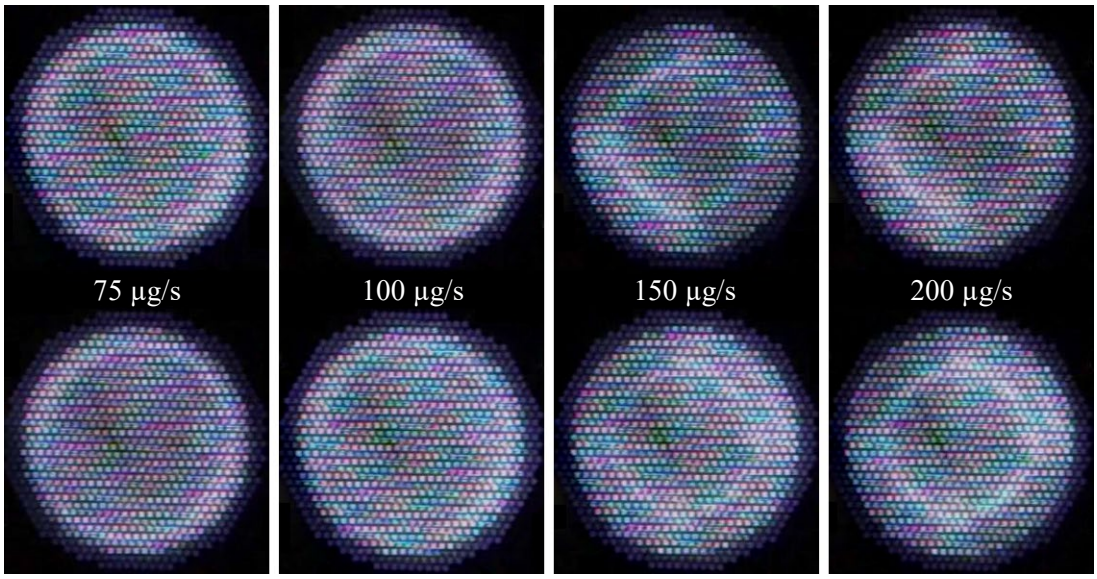

Fig. 8 Argon Discharge Variance with Flowrate. Top Row: Mean P_{abs} = 5.72 W (σ = 0.18). Bottom Row: Mean P_{abs} = 19.35 W (σ = 0.57).

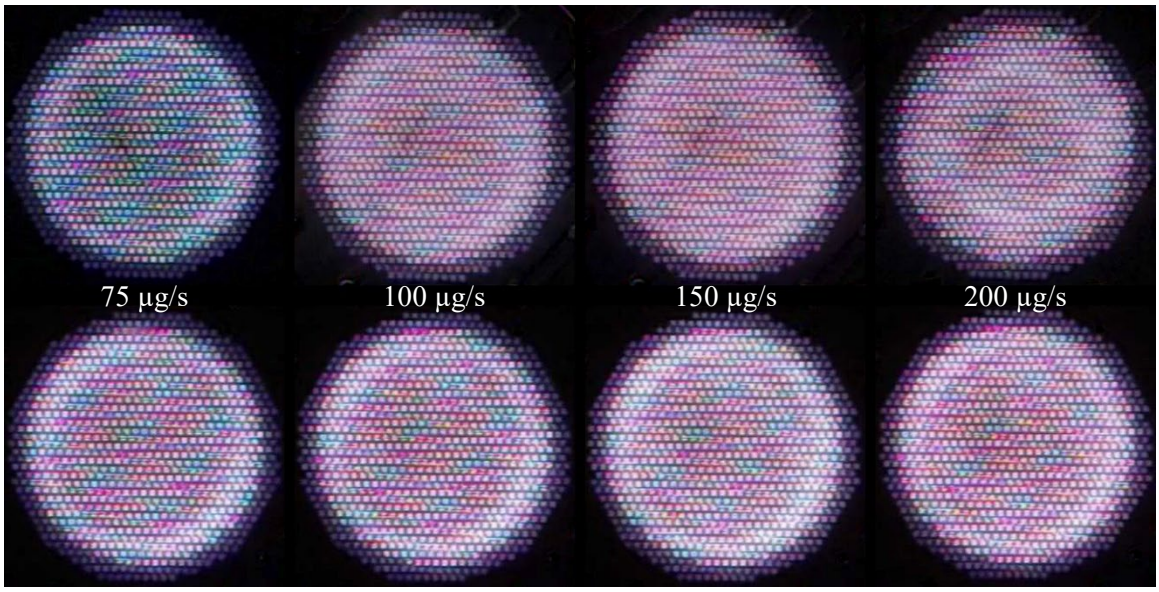

Fig. 9 Top Row: Nitrogen Discharge Mean P_{abs} = 19.52 W (σ = 0.35). Bottom Row: Air Discharge Mean P_{abs} = 19.32 W (σ = 0.47).

2. Light Intensity Comparison

The plasma discharge asymmetry observed above relates not only to the mass flowrate, but also to the propellant species. For comparison, plasma discharge images were imported into ImageJ, converted into 16-bit gray scale images, and the light intensity extracted across the apertures centered along the front of the thruster. Fig. 10 presents light intensity plots for flowrates of 75 µg/s and 200 µg/s with P_{abs} of approximately 20 W. For the 200 µg/s case, all three propellant species show symmetry across the thruster centerline with respect to peak gray values. For the 75 µg/s case, both argon and nitrogen have peak values at -38.1 mm but differing positions on the positive side of the centerline while the position of peak values for air is at ± 41.6 mm. However, this alone does not suffice to account for characterization of the discharge variance and in an effort to better elucidate the trends we introduce a flatness parameter with respect to the gray value of light intensity similar to the beam current flatness parameter [11]. We define the light intensity flatness parameter as

$$f_{gray} = \frac{1}{r_0 I_{gray,max}} \int_0^{r_0} I_{gray}(r) dr \tag{4}$$

where r_0 is the radius of the open area of the ion optics, $I_{gray,max}$ is the maximum light intensity value for a particular propellant, flowrate, and P_{abs}, and $I_{gray}(r)$ is the spatial variation in light intensity. A value of 1 would represent a square or flat light intensity profile, while a value of 0 is a delta function at some radial position. Fig. 11 presents the flatness parameter values for all three propellants at 75 and 200 µg/s flowrates. The azimuthal angles specified in Fig. 11 are relative to the azimuthal location of the monopole antenna inside the waveguide. The tabulated flatness parameters were calculated based on a line integral starting from the thruster centerline and moving outward. For clarity, the flatness parameters at angles of 0° and 180° correspond to the aperture averaged values depicted in Fig. 10. The 0° azimuthal location (the azimuthal location of the antenna) is the positive side of the X-axis, while the 180° azimuthal location is the negative side of the X-axis.

Comparison of the data presented in Fig. 11 demonstrates a general decrease in flatness parameter with increasing angle from 0° to 180° followed by an increase above 180°. This trend is pronounced in the 75 µg/s case for all three propellants with argon presenting the greatest variation. In the 200 µg/s case, argon again shows a greater range in flatness parameter than the other two gases which comparatively flatten; both in respect to argon at 200 µg/s and to their results at 75 µg/s. Therein is the other key takeaway from this analysis: higher flowrate denotes an overall higher flatness parameter for both nitrogen and air, however, this is not the case with argon which saw a greater divergence in flatness at the increased flowrate condition.

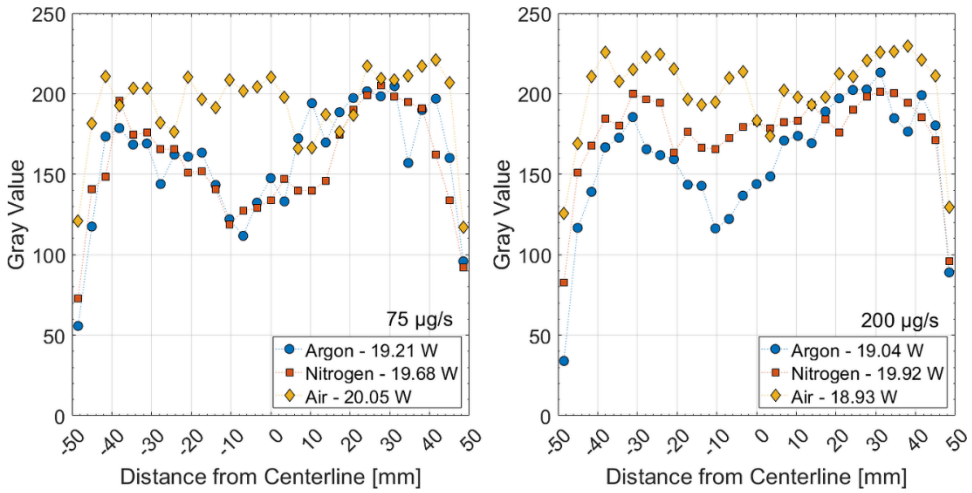

Fig. 10 Light intensity across thruster face. Left: 75 µg/s. Right: 200 µg/s.

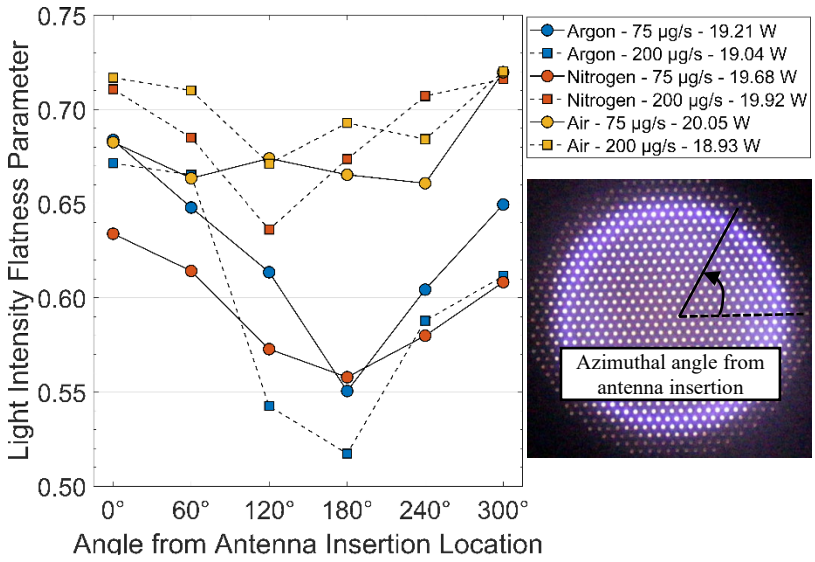

Fig. 11 Light Intensity (Gray Value) Flatness Parameter vs Azimuthal Angle from Antenna Insertion.

B. Downstream Plasma Properties

For a more direct comparison between propellant types, experimental results were compared based upon the mass flowrate normalized by absorbed microwave power. This approach was employed by Sheppard and Little for comparison of propellant species within the context of an ECR magnetic nozzle thruster [6]. Fig. 12 and Fig. 13 present the mean and range of values for electron temperature and electron number density, respectively.

1. Electron Temperature

The plots shown in Fig. 12 and Fig. 13 are for a subset of data taken at apertures ±17.3 mm and ±27.7 mm off the centerline of the thruster in a single plane. In terms of electron temperature, the trends observed for argon and air are similar to those reported by Sheppard and Little in 2022: T_e increases with decreasing $\dot{m}/P_{abs}$. Moreover, T_e is more strongly associated with the input mass flowrate than with $\dot{m}/P_{abs}$, but this result is expected given the shorter mean free path inside the PDC at higher flowrates. In general, the temperature observed was consistent at any particular flowrate. However, the nitrogen case is comparatively dissimilar as there is a notable increase in T_e with increasing $\dot{m}/P_{abs}$. The greatest deviance observed is for the 150 µg/s flowrate data, particularly at $\dot{m}/P_{abs}$ = 26.7 µg/J. Despite this inverse response, the T_e results are consistent with respect to flowrate for the 75, 100, and 200 µg/s cases.

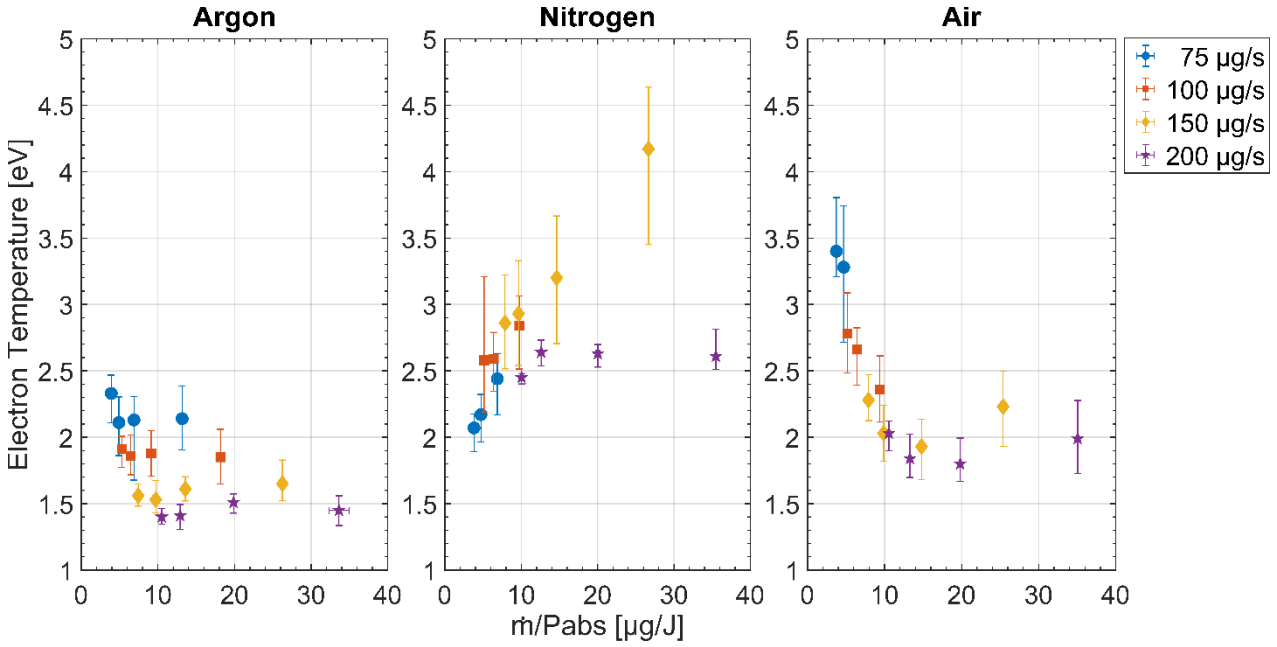

Fig. 12 Electron Temperature vs Mass Flowrate Normalized by Absorbed Microwave Power.

2. Number Density

The number density of electrons similarly increases with decreasing $\dot{m}/P_{abs}$ for argon and nitrogen but presents a local maxima between 10 to 15 µg/J for air. Additionally, there is a greater correlation between electron density and $\dot{m}/P_{abs}$ than with flowrate alone for nitrogen and air. In contrast, argon results denote higher densities at higher flowrates for comparable values of $\dot{m}/P_{abs}$.

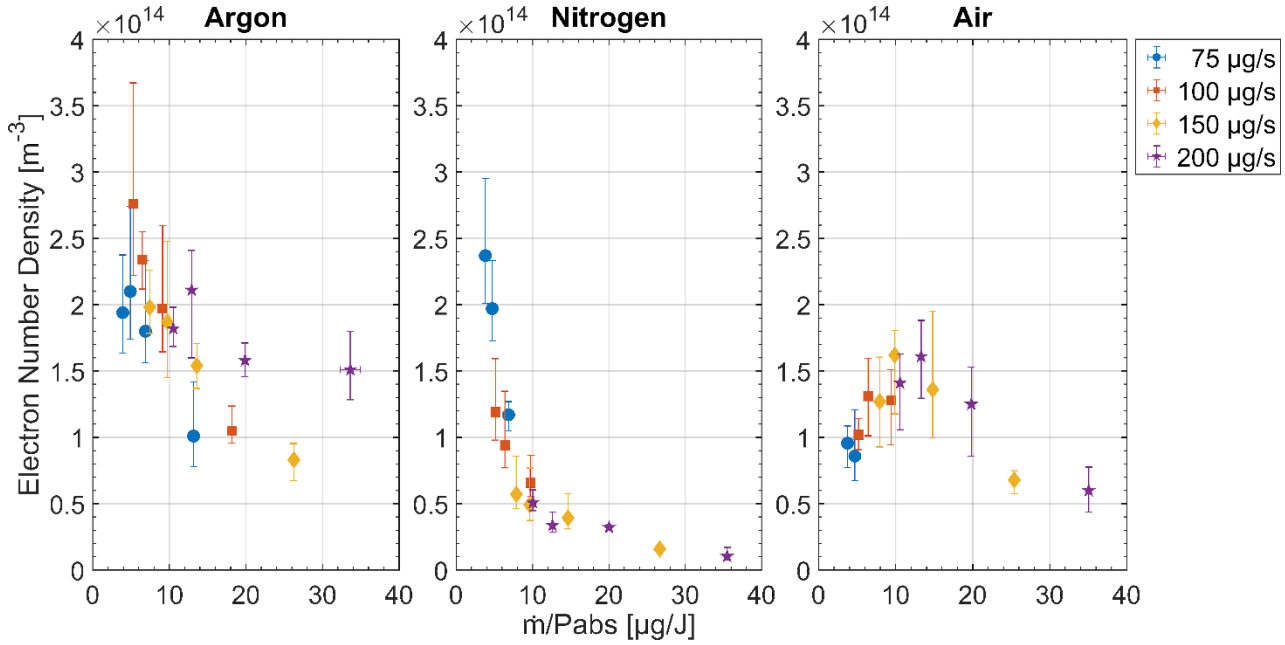

Fig. 13 Electron Number Density vs Mass Flowrate Normalized by Absorbed Microwave Power.

IV. Plasma Light Emission Correlation with ECR Zones

The spatial variation of light emissions, as observed through the ion optics, was compared with the expected ECR zones in the PDF. This approach was also considered by Fu and Ding in their 2021 study [22]. This approach to analyzing plasma through the light emission rests on the assumption that light intensity is to first order representative of plasma density. Fig. 14 presents the same magnetic field contour plot first shown in Fig. 4 with an overlayed plot of the gray value corresponding to light emitted by an argon discharge at individual apertures. The gray intensity value has been normalized to the peak intensity of each curve. The circle markers are for 75 µg/s at P_{abs} = 5.70 W while the square markers are for 200 µg/s at P_{abs} = 5.95 W. The lowest P_{abs} cases were chosen for plotting as they present lower levels of light saturation and therefore allow for a better indication of the individual intensity through a single aperture. The overlaid black and white highlights in Fig. 14 occur at the local maximum values on either side of the centerline and help elucidate the spatial variation with propellant flowrate. Light intensity maxima for the 75 µg/s case occur at -38.1 mm and 41.6 mm (large radius plasma ring), while the maxima for the 200 µg/s case occur at ±31.2 mm (smaller radius plasma ring) off the centerline. The location of the light intensity maxima are well aligned with the ECR field lines for the incident microwave frequency. The smaller diameter plasma ring observed at 200 µg/s is aligned with the ECR field lines further upstream from the screen grid, which corresponds to a discharge inside and near the exit of the 74 mm diameter waveguide. In contrast, the 75 µg/s case shows alignment more closely to the ECR field line nearer the screen grid, which in terms of performance is the preferred discharge location as noted by Yamashita et al. [21]. While this optical approach cannot directly account for the depth at which the plasma is formed and distributed, the radial position of the discharge as given by the visual ring light intensity is shown to agree quite well with the experimentally mapped magnetic field inside the PDC.

The last major takeaway from Fig. 14 is the asymmetry of the light intensity with respect to the thruster centerline. This aspect of the plasma discharge has been observed in the beam current profile of the redesigned version of the µ10 thruster as reported by Tani et al. in 2019 [11]. Fig. 14 shows a larger normalized light intensity on the positive side of the X-axis as compared to the negative side. This is attributed to the location of the monopole antenna, which is mounted on the right side (relative to the plot) of the waveguide. Unfortunately, the oversaturation of light intensity, and lack of a stable discharge precludes comparison for nitrogen and air at this time. Analysis of other propellants in the future will further elucidate the main parameters affecting discharge variability in this ECR thruster type.

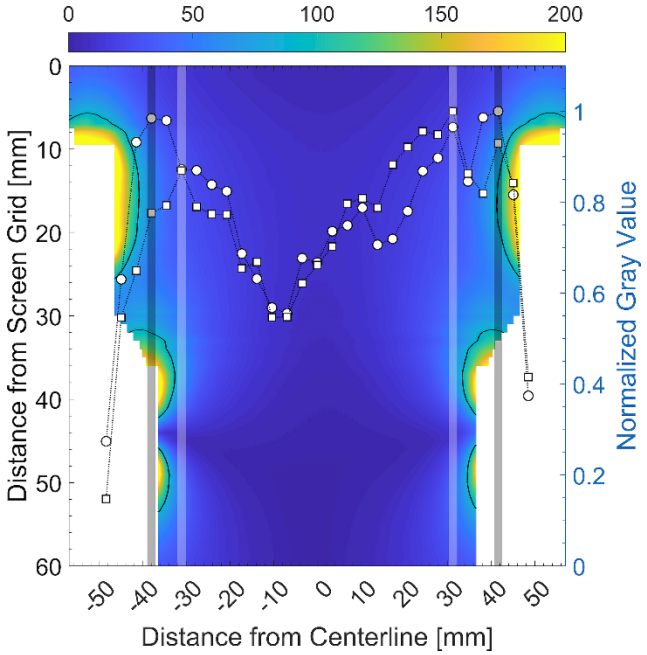

Fig. 14 Magnetic Field Strength Contour Plot with Comparison of Normalized Gray Value of Argon Discharge. Circle Markers: 75 µg/s at 5.70 W. Square Markers: 200 µg/s at 5.95 W.

V. Beamlet Trajectory Modeling

Simulation of gridded ion optic systems is a fairly mature field, and simulation codes have been developed that are powerful and accurate [24,25]. In lieu of developing a bespoke software package, we opt to use SIMION to simulate ion trajectories. SIMION is a software package that is primarily used to calculate electric fields and simulate trajectories of charged particles based on inputs magnetic field and electrical potential. SIMION allows for programmatic input of electrode geometries, along with flexible user programs written in Lua to cater to specific needs. This is helpful for iterating the design of optics by allowing for rapid change of electrode geometry, extraction potentials, and ion species. The standard version of SIMION solves the Laplace equation and ignores space charge, however, in this study, the Poisson Code has also been used which iteratively approximates the space charge effect in a beam. The following sections discuss the setup for the simulation and the code structure. Then, we validate our model against existing models both qualitatively and quantitatively. Beamlet trajectory results for xenon, argon, nitrogen, and oxygen are described for a range of beamlet currents and different optics geometries.

A. Simulation Model

SIMION offers multiple options when deciding the symmetry and mirroring options of the simulation space. Given the symmetry of ion optics systems, a 2D cylindrical system has been used in this study. The axial and radial distances of the simulation space are dependent on the ion optics being simulated. As a rule of thumb, the radial distance simulated is equal to the screen grid aperture radius rounded up to the nearest millimeter. The axial distance simulated must be sufficient such that the trajectory of the beamlet after exiting the ion optic system can be characterized. A fine rectangular mesh where 1mm = 100 grid units (gu) in every axis has been used for all simulation cases.

SIMION accepts electrode geometry and electric potentials in GEM files and Dirichlet boundary conditions are applied to these electrodes. In this model, we approximate the plasma as an electrode at a constant plasma potential V_{plasma} and screen and accelerator electrodes at V_s and V_a, respectively. Finally, we define a 1 gu thick neutralizer electrode at 0 V potential at the downstream boundary of the simulation space. Usually, V_{plasma} is tens of volts higher than V_s, however, this difference in potential is negligible compared to the extraction potential V_{ext}. Therefore, to reduce complexity, the plasma potential is always taken to be 20 V higher than V_s. The boundaries of the simulation space that are not defined as electrodes are automatically assigned a Neumann boundary condition. The simulation space along with the electrode definitions and boundary conditions are shown in Fig. 15 with the green lines representing individual ion trajectories, red lines are equipotential lines, and the brown meshed structures are the electrodes.

The shape of the plasma meniscus has a considerable effect on the ion beamlet trajectory and is usually determined numerically. To reduce complexity, an analytically derived meniscus shape is used in this simulation model as a first order approximation. The meniscus shape is assumed to be spherical and is always attached to the triple point connecting the bulk plasma, the screen electrode, and the non-electrode ion acceleration region. With this approach the only parameter required to fully define the plasma meniscus shape is its radius. To do this, we use the Langmuir-Blodgett formalism [26,27], which describes solutions to the Poisson's equation for space-charge limited flow between concentric spherical electrodes. Because we can approximate the flat electrodes as spherical electrodes with large radii, this formalism can be used to analytically find the meniscus shape when ions are extracted from bulk plasma through parallel flat electrodes. The divergence of beam at the plasma meniscus θ is defined as:

$$\boldsymbol{\theta \cong 0.625 \frac{r_s}{d}\left(1 - \frac{P}{P_{pp}}\right)} \tag{5}$$

where r_s is the radius of the screen grid aperture and d is the distance between the upstream faces of the screen and accelerator electrodes. Therefore,

$$\boldsymbol{d = t_s + l_g} \tag{6}$$

where t_s is the thickness of the screen electrode and l_g is the grid gap. In Equation (5)(5, perveance P is defined as:

$$\boldsymbol{P = \frac{I}{V_{ext}^{3/2}}} \tag{7}$$

and the Child-Langmuir perveance P_{pp} is defined as:

$$P_{pp} = \frac{4}{9}\epsilon_0 \left(\frac{r_s}{d}\right)^2 \sqrt{\frac{2q}{M}} \tag{8}$$

where I is the beamlet current being extracted, ϵ_0 is the permittivity of free space, q is the elementary charge, and M is the molecular mass of the extracted ion species. We can also use θ to back out the meniscus radius r_{men} based on the following equation.

$$r_{men} = \frac{r_s}{\sin\theta} \tag{9}$$

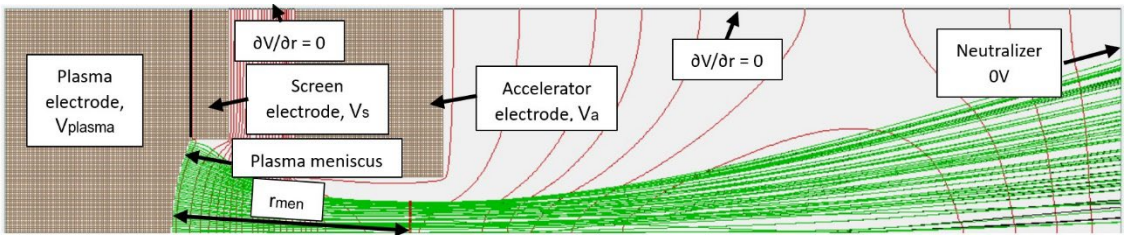

Fig. 15 2D Simulation Space.

In this simulation, 100 ions are used to define the entire beam. While more or less ions may be used, it has been shown that 100 ions gives results with sufficient fidelity at low computation times. The ion initial positions are equally spaced within the screen grid aperture diameter in the Y-axis and 1 gu to the right of the plasma meniscus in the X-axis. As all ions are in the XY-plane the Z-position of all the ions is zero.

All ions have an initial velocity pointing towards a point in the center of the sphere defining the plasma meniscus with the initial energy determined using the Bohm criterion [28,29]. The Bohm criterion states that ions must fall through a potential of at least $T_e/2$ before entering the plasma sheath, where T_e is the electron temperature in the bulk plasma. Therefore, we define the ion initial energies to be the theoretical maximum possible energy: $T_e/2$. The corresponding speed of each ion is the acoustic velocity for cold ions which is defined as follows:

$$v_0 = \sqrt{\frac{kT_e}{M}} \tag{10}$$

where k is the Boltzmann constant.

B. Code Structure

As previously mentioned, SIMION's Poisson solver has some additional requirements. To account for space charge, an additional empty potential array (PA) file is required, the name and size of which must be compatible with the PA file containing the electrode definitions. In the workbench (IOB) file, the space charge PA file must be given higher priority over the electrode PA file.

A SIMION workbench file is written which is executed during the simulation run. The *palib* and *piclib* libraries have been already defined among the examples provided with SIMION 8.1, which have been used to create this workbench file. The *palib* provides extensive programmatic functionality and is a Particle-in-Cell (PIC) library that makes writing and executing the workbench file much easier. The workbench file is used to set the parameters of the code, such as the number of iterations, convergence tolerance, and current start ratio. Importantly, this file is also used to define the amount of current passed by each ion. The average amount of current passed through each ion is calculated by dividing the total beamlet current I by the number of ions. The current carried by each ion is weighted by y/r_{mean}, where y is the initial y-distance of the ion and r_{mean} is $0.5r_s$. Each ion is initialized as such in the workbench program. Finally, the *current* module in *piclib* is called to execute the rest of the code under the hood. A version of the workbench file is provided within the example files of SIMION 8.1.

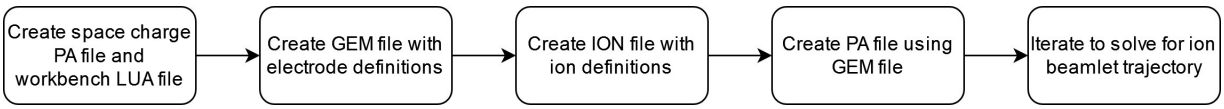

Fig. 16 Code setup and operation chart.

The *piclib* library contains two main modules: the *charge* module and the *current* module. The *charge* module is useful in the case of time dependent charge repulsion while the *current* module is useful in the case of time independent charged-particle beams. Because ion extraction falls under the second category, we shall only be discussing the *current* module under *piclib*. The *current* module first solves electric potential at every non-electrode point by executing a 'refine' function that solves the Poisson equation. Next, the code initializes all the ions using the weights defined in the workbench files. Then the ions are then flown based on the ion initial conditions defined in the ION file, and the potential field calculated in the refine step is used to calculate the forces acting on each ion at each time step. For each time step, the charge deposited by individual ions is added to a charge density array. Charge deposited in a grid unit is defined as the product of the current being carried by the relevant ion and the length of the time step being used in the simulation. A smoothing function is applied to the charge density distribution spatially, and after all the ions either exit the simulation space or collide with an electrode in the current iteration, the charge density array is used to define the space charge PA for the next iteration. Then, the electrode PA and the new space charge PA are used to solve for the potential distribution by refining. The entire process is repeated until the specified iterations are executed. The ion beamlet trajectory from the second to last iteration is not erased after the next iteration begins so that we can visually check for convergence of solution by comparing it to the beamlet trajectory calculated in the last iteration. In all beamlet trajectory images, the green trajectories are the ones calculated in the last iteration, while the underlying black trajectories are the ones calculated in the previous iteration.

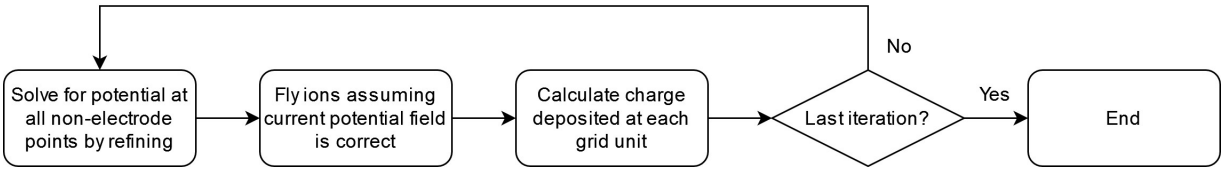

Fig. 17 Iterative process to solve for beamlet trajectory implemented in *piclib*.

C. Code Validation

Simulation cases from literature have been rerun using our ion optics simulation code to validate our model. Qualitative comparisons are made by comparing the final beamlet trajectory and potential distribution against those reported in literature. Quantitative comparisons are also made where, for a specific simulation case, the impingement versus beamlet current curve found using our model is compared to that reported in literature.

1. Qualitative Comparisons

For qualitative comparisons, we have simulated two cases from [30] where the beamlet trajectories are reported. The plasma properties, beamlet current, and geometric parameters of the electrodes are listed in Table 3. Fig. 18a and Fig. 19a are the beamlet trajectories reported in [30] for the two cases in Table 3. Fig. 18b and Fig. 19b are the beamlet trajectories obtained using our simulation model. We see that there is good agreement between the two sets of results when we look at the meniscus shape, the final beam divergence, the far-field beam radius, and the potential field.

Table 3 Simulated Geometry and Operating Conditions for Qualitative Comparison

Case	Species	T_e [eV]	I [mA]	r_s [mm]	r_a [mm]	t_s [mm]	t_a [mm]	l_g [mm]	V_s [V]	V_a [V]
1	Xe	2.4	2.06	2.00	1.50	0.50	2.50	1.50	4500	-500
2	Xe	5.0	0.48	1.25	0.80	0.50	2.00	0.90	2000	-215

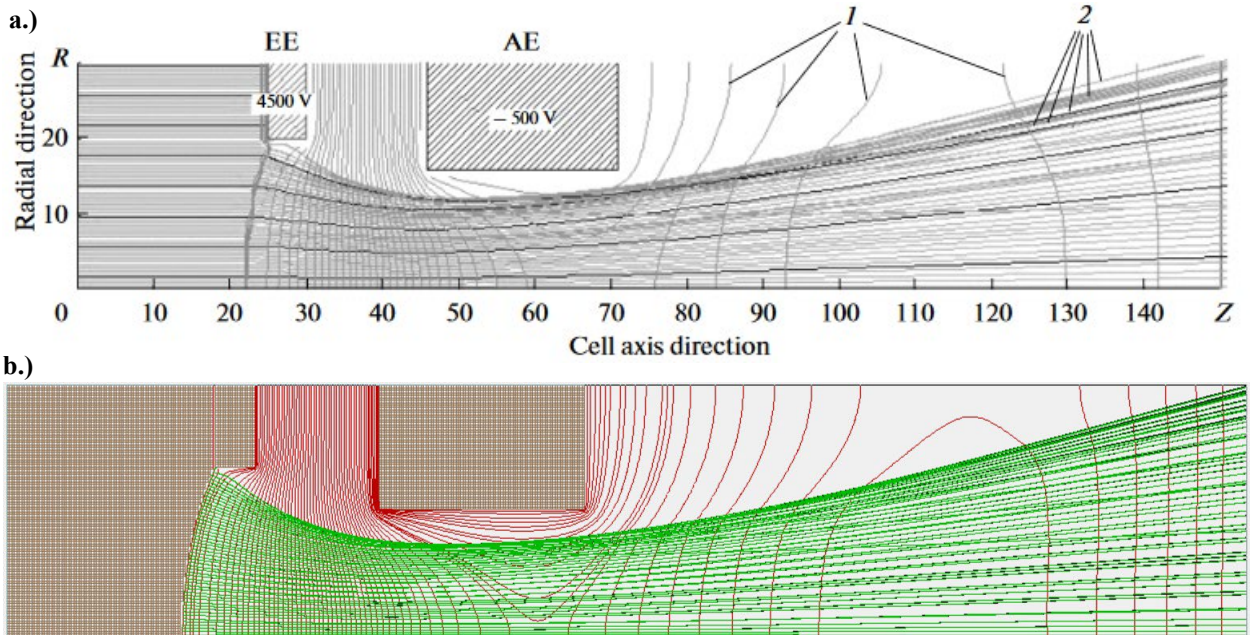

Fig. 18 Ion Beamlet Trajectory and Potential Contours for Simulation Case 1 a) literature results from Ref [30] b) using our SIMION model.

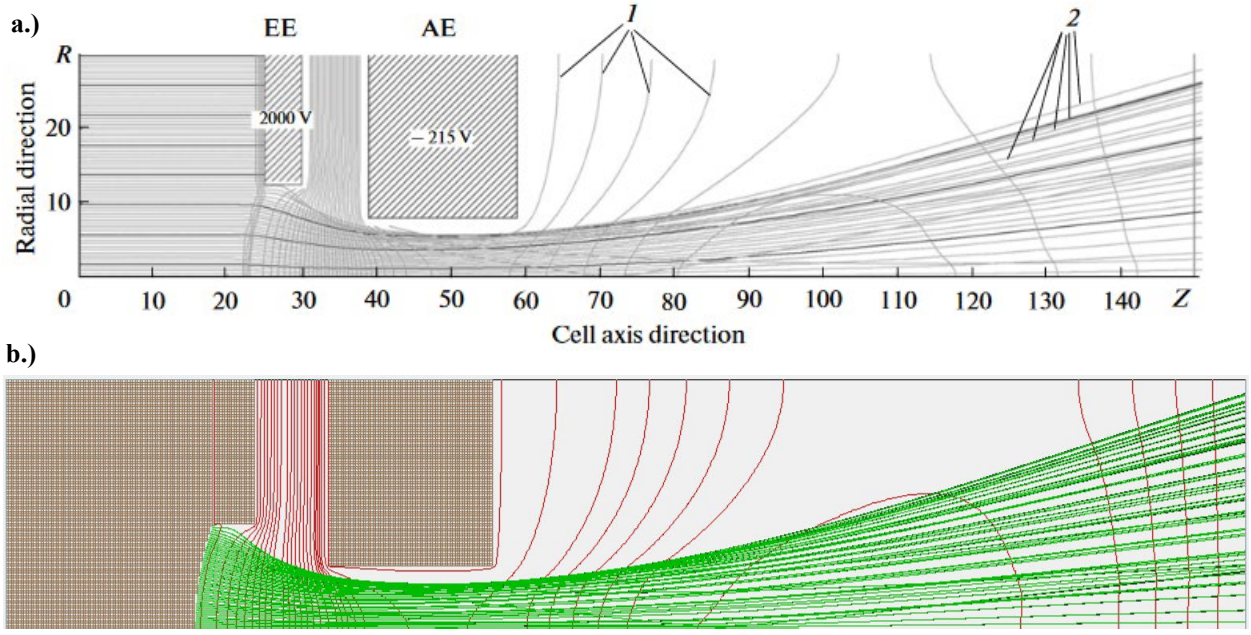

Fig. 19 Ion Beamlet Trajectory and Potential Contours for Simulation Case 2 a) literature results from Ref [30] b) using our SIMION model.

2. Quantitative Comparisons

We quantitatively compared the impingement versus beamlet current data from our model with one reported [31]. The impingement percentage as a function of beamlet current generated using our model is plotted in Fig. 20 with the impingement percentage calculated as follows:

$$\boldsymbol{Impingement}\ \% = \frac{\boldsymbol{I_{imp}}}{\boldsymbol{I}} \times \mathbf{100}\% \tag{11}$$

where I_{imp} is the beamlet current impinging on the acceleration grid, and I is the total beamlet current through the screen grid. The corresponding data for comparison is taken from Figure 10 of the reference [31]. The geometric parameters and operating conditions of the electrode used for quantitative analysis are provided in Table 4.

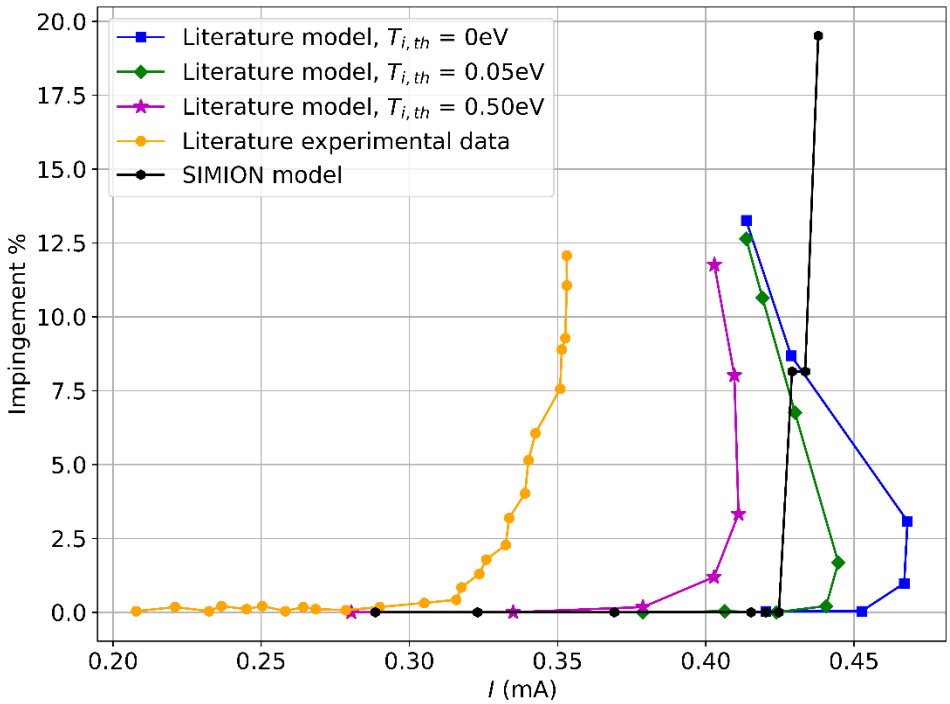

Fig. 20 Impingement % vs *I* for quantitative comparison.

Table 4 Simulated Geometry and Operating Conditions for Qualitative Comparison

Propellant Species	T_e [eV]	r_s [mm]	r_a [mm]	t_s [mm]	t_a [mm]	l_g [mm]	V_s [V]	V_a [V]
Xe	5.0	1.150	0.70	0.45	1.00	0.80	1570	-176

One of the assumptions taken in our model is cold ions that originate at their acoustic velocity. This means that in our model, the bulk plasma ion temperature is 0 eV. The perveance limit calculated by our model is near identical to that calculated by the literature model for the low ion thermal temperature cases of 0eV and 0.05eV. We see large increases in impingement percentage with small increases to the beamlet current, which we believe is an artifact of the discretized nature of the simulated beamlet. However, this comparison also brings to light a limitation of our model. With low ion beamlet currents, impingement due to beamlet crossover is expected, as is reported in literature [31], but there is no impingement recorded with low beamlet currents in our model.

D. Grid Geometry Case Study

In this section, we consider three grid geometries and study the performance of four different propellants: xenon, argon, nitrogen, and oxygen. The nitrogen and oxygen beams are assumed to comprise entirely of N_2^+ and O_2^+ respectively. The grid dimensions investigated are the same as the grids being used experimentally with the only difference between the three cases being the grid gap between the screen and acceleration grids. The grid geometries and the operating conditions simulated are outlined in Table 5.

Table 5 Simulated Geometry and Operating Conditions for Case Study

Species	T_e [eV]	r_s [mm]	r_a [mm]	t_s [mm]	t_a [mm]	l_g [mm]	V_s [V]	V_a [V]
Xe, Ar, N_2, O_2	5.0	1.525	0.60	0.50	0.50	0.50, 1.0, 1.50	1500	-350

Normalized perveance per unit hole area [24] is defined in Equation 12, which can be used to measure the relative ion extraction compared to the theoretical maximum possible amount of ion extraction,

$$P_{TG} = \frac{I}{A}\frac{l_e^2}{V_{ext}^{3/2}}\left(\frac{4}{9}\epsilon_0\sqrt{\frac{2q}{M}}\right)^{-1} \tag{12}$$

where A is the open screen grid hole area and l_e is the effective grid spacing. Both of which are specified below.

$$A = \pi r_s^2 \tag{13}$$

$$l_e = \sqrt{(t_s + l_g)^2 + r_s^2} \tag{14}$$

As stated previously, I is the beamlet current, V_{ext} is the extraction potential, ϵ_0 is the permittivity of free space, q is the elementary charge, and M is the molecular mass of the ion species extracted.

1. Simulated Case Study Results

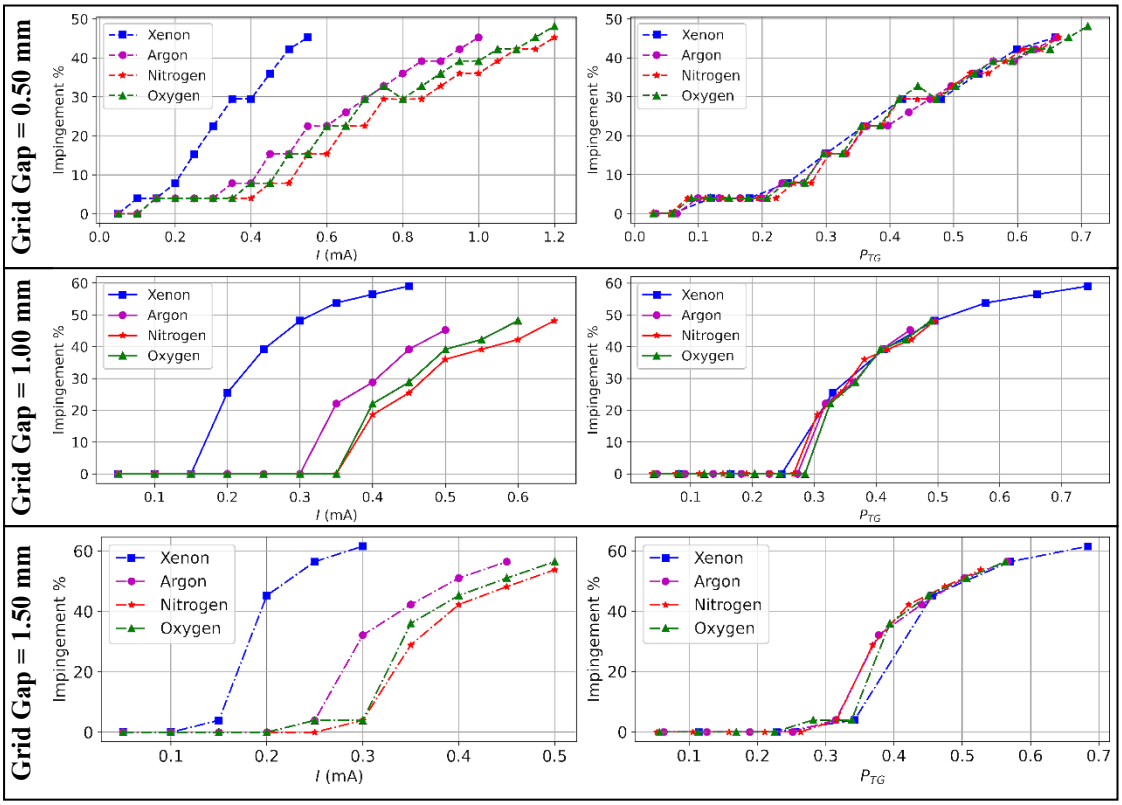

Fig. 21 Impingement% VS Left Column: *I*. Right Column: P_{TG}.

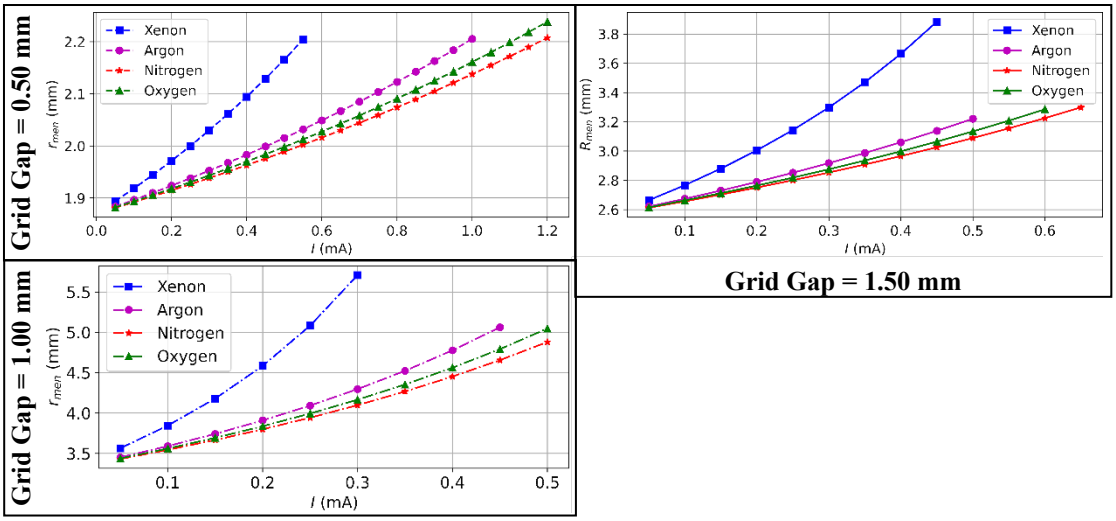

Fig. 22 Meniscus Radius (r_{men}) vs *I*.

2. Simulation Discussion

The meniscus radius increases as the grid gap increases for all propellant species. That means, with a larger grid gap, the beam becomes flatter, leading to perveance limit being reached at lower beamlet currents. For each grid gap, propellants with higher molecular mass correspond to larger meniscus radii and lower perveance limits. For each grid gap, all four propellants have identical impingement percentage versus P_{TG} curves. As noted, this model does not accurately predict crossover impingement as it shows no impingement at low beamlet currents.

VI. Conclusions

The results of this study provide an initial picture of the plasma discharge properties inside an ECR microwave thruster, which demonstrates the further feasibility of myriad propellant types. The downstream properties of the plasma discharge were evaluated for $\dot{m}/P_{abs}$ ranges of 3.91 to 33.6 µg/J for argon, 3.81 to 35.5 µg/J for nitrogen, and 3.74 to 35.06 µg/J for air. Results for argon present electron temperature ranges from 1.40 to 2.33 eV with a corresponding number density range of $8.3x10^{13}$ to $2.8x^{14}$ m^{-3}. Nitrogen results presented a range of electron temperatures from 2.1 to 4.1 eV and number densities of $1.04x10^{13}$ to $2.4x10^{14}$ m^{-3} while air discharges spanned electron temperatures of 1.8 to 3.4 eV and number densities of $6.0x10^{13}$ to $1.6x10^{14}$ m^{-3}. Electron temperature results denote similar trends observed with $\dot{m}/P_{abs}$ in literature for argon and air propellants. Dissimilar results are evident using nitrogen which require further examination as this result could either be due to experimental error or some currently uncaptured trend. With respect to the plasma density measured outside of the PDC, air presents a peak electron density at approximately 12 µg/J, while argon and nitrogen demonstrate the more common trend of increasing density with decreasing $\dot{m}/P_{abs}$.

Light emissions from the plasma were considered for mass flowrates of 75 and 200 µg/s which demonstrate the asymmetry of the discharge. Air presents the greatest symmetry with peak values on either side of the thruster centerline at ±41.6 mm for the 75 µg/s case, and ±38.1 mm for the 200 µg/s case. In contrast, peak values for argon were observed at -38.1 mm and 31.2 mm for the 75 µg/s case while nitrogen values peaked at -38.1 mm and 27.7 mm. For the 200 µg/s case, both argon and nitrogen had peak values at ±31.2 mm. To further evaluate discharge asymmetry, we have introduced a flatness parameter with respect to the light emission and angle off the insertion point of the monopole antenna. This flatness parameter was again considered for the 75 and 200 µg/s flowrate cases. Trends indicate a reduction in flatness with an increasing angle up to 180° with argon showing the most pronounced reductions. For the 75 µg/s case, argon showed a mean flatness parameter of 0.63 (σ = 0.046) with nitrogen and air having 0.60 (σ = 0.029) and 0.68 (σ = 0.022), respectively. In the 200 µg/s case, argon, nitrogen, and air have values of 0.60 (σ = 0.063), 0.69 (σ = 0.03) and 0.70 (σ = 0.02), respectively. Comparison of the plotted light intensity seen through the apertures of the ion optics overlayed on the experimentally mapped permanent magnetic field inside the PDC demonstrate good alignment with respect to the field strength at the ECR condition.

Further investigation is required to provide a more comprehensive view of the discharge properties of alternative propellants in the microwave ECR thruster presented. The key issues to be addressed are profiling the discharge

properties inside the PDC with particular interest in spatial variance (both radially and depth-wise), expansion of propellant species and the $\dot{m}/P_{abs}$ range investigated, high resolution imaging and light intensity profiling for all operating parameters, and a more fundamental investigation of microwave propagation through the waveguide and PDC in the presence of the spatially varying plasma.

Additionally, we have developed a simple code to simulate ion beamlet trajectories through ion optics. This code was developed to be run on top of the SIMION software package. This code has been validated qualitatively and quantitatively against existing literature, and it has been demonstrated that the results are close to those reported at beamlet currents close to the perveance limit. Next, using this code, we have simulated the performance of four different alternative propellants through three different ion optics configurations. There are future improvements to be made to this model, including numerically solving for the meniscus shape for accurate results at ion beam crossover. Simulating surrounding beamlets would make this code accurately simulate 3-dimensional effects and improve fidelity. A more accurate version of this model shall be used to design optimal ion optics for alternative propellants of interest.

Acknowledgments

The authors would like to acknowledge funding and technical support from Lockheed Martin Corporation. The authors would also like to thank Dr. Hiroyuki Koizumi for his valuable insight and words of encouragement during the development of the ECR thruster.

References

[1] Petro, E. M., and Sedwick, R. J., "Effects of Water-Vapor Propellant on Electrodeless Thruster Performance," *Journal of Propulsion and Power*, Vol. 33, No. 6, 2017, pp. 1410–1417. https://doi.org/10.2514/1.B36389

[2] Nakamura, K., Koizumi, H., Nakano, M., and Takao, Y., "Effects of Negative Ions on Discharge Characteristics of Water Plasma Source for a Miniature Microwave Discharge Ion Thruster," *Physics of Plasmas*, Vol. 26, No. 4, 2019, p. 043508. https://doi.org/10.1063/1.5092754

[3] Koizumi, H., Asakawa, J., Nakagawa, Y., Nishii, K., Takao, Y., Nakano, M., and Funase, R., "Assessment of Micropropulsion System Unifying Water Ion Thrusters and Water Resistojet Thrusters," *Journal of Spacecraft and Rockets*, Vol. 56, No. 5, 2019, pp. 1400–1408. https://doi.org/10.2514/1.A34407

[4] Sheppard, A. J., and Little, J. M., "Scaling Laws for Electrodeless Plasma Propulsion with Water Vapor Propellant," *Plasma Sources Science and Technology*, Vol. 29, No. 4, 2020, p. 045007. https://doi.org/10.1088/1361-6595/ab759e

[5] Gallagher, H. E., "Poisoning of LaB6 Cathodes," *Journal of Applied Physics*, Vol. 40, No. 1, 2003, pp. 44–51. https://doi.org/10.1063/1.1657092

[6] Sheppard, A. J., and Little, J. M., "Performance Analysis of an Electron Cyclotron Resonance Thruster with Various Propellants," *Journal of Propulsion and Power*, Vol. 38, No. 6, 2022, pp. 998–1008. https://doi.org/10.2514/1.B38698

[7] Barquero, S., Tabata, K., Tsukizaki, R., Merino, M., Navarro-Cavallé, J., and Nishiyama, K., "Performance Characterization of the M10 Electron-Cyclotron-Resonance Ion Thruster Using Alternative Propellants: Krypton vs. Xenon," *Acta Astronautica*, Vol. 211, 2023, pp. 750–754. https://doi.org/10.1016/j.actaastro.2023.06.036

[8] Barquero, S., Tabata, K., Tsukizaki, R., Merino, M., Navarro-Cavallé, J., and Nishiyama, K., "Alternative Propellant Study (Krypton vs. Xenon) of the M10 ECR Gridded Ion Thruster at Its Hayabusa2 and DESTINY+ Missions."

[9] Moloney, R., Karadag, B., Fabris, A., Staab, D., Frey, A., Garbayo, A., Shadbolt, L., Rosati Azevedo, E., Faircloth, D., Lawrie, S., and Tarvainen, O., "Experimental Validation and Performance Measurements of an ECR Thruster Operating on Multiple Propellants," 2019.

[10] Vialis, T., Jarrige, J., and Packan, D., "Geometry Optimization and Effect of Gas Propellant in an Electron Cyclotron Resonance Plasma Thruster IEPC-2017-378," 2017.

[11] Tani, Y., Tsukizaki, R., Koda, D., Nishiyama, K., and Kuninaka, H., "Performance Improvement of the M10 Microwave Discharge Ion Thruster by Expansion of the Plasma Production Volume," *Acta Astronautica*, Vol. 157, 2019, pp. 425–434. https://doi.org/10.1016/j.actaastro.2018.12.023

[12] Boye, C., Navarro Cavallé, J., and Merino-Martinez, M., "Preliminary Analysis of the Magnetic Arch Plasma Expansion in a Cluster of Two ECR Plasma Thrusters," 2023. https://doi.org/10.13009/EUCASS2023-681

[13] Li, Y., Tang, H., Cai, G., Fu, C., and Wang, W., "Radio-Frequency Biasing of Ion Acceleration Grids with Different Propellants," *Plasma Sources Science and Technology*, Vol. 31, No. 3, 2022, p. 035009. https://doi.org/10.1088/1361-6595/ac525b
[14] Vinci, A. E., and Mazouffre, S., "Direct Experimental Comparison of Krypton and Xenon Discharge Properties in the Magnetic Nozzle of a Helicon Plasma Source," *Physics of Plasmas*, Vol. 28, No. 3, 2021, p. 033504. https://doi.org/10.1063/5.0037117
[15] Nakagawa, Y., Koizumi, H., Naito, Y., and Komurasaki, K., "Water and Xenon ECR Ion Thruster—Comparison in Global Model and Experiment," *Plasma Sources Science and Technology*, Vol. 29, No. 10, 2020, p. 105003. https://doi.org/10.1088/1361-6595/aba2ac
[16] Nakamura, K., Nakagawa, Y., Koizumi, H., and Takao, Y., "Numerical Analysis of a Miniature Microwave-Discharge Ion Thruster Using Water as the Propellant," *TRANSACTIONS OF THE JAPAN SOCIETY FOR AERONAUTICAL AND SPACE SCIENCES*, Vol. 61, No. 4, 2018, pp. 152–159. https://doi.org/10.2322/tjsass.61.152
[17] Ataka, Y., Nakagawa, Y., Koizumi, H., and Komurasaki, K., "Improving the Performance of a Water Ion Thruster Using Biased Electrodes," *Acta Astronautica*, Vol. 187, 2021, pp. 133–140. https://doi.org/10.1016/j.actaastro.2021.06.020
[18] Nishii, K., Koizumi, H., and Komurasaki, K., "Experimental Characterization of Nozzle Performance at Low Reynolds Numbers for Water Microthrusters," *Journal of Propulsion and Power*, Vol. 37, No. 4, 2021, pp. 595–603. https://doi.org/10.2514/1.B38147
[19] Tsukizaki, R., Ise, T., Koizumi, H., Togo, H., Nishiyama, K., and Kuninaka, H., "Thrust Enhancement of a Microwave Ion Thruster," *Journal of Propulsion and Power*, Vol. 30, No. 5, 2014, pp. 1383–1389. https://doi.org/10.2514/1.B35118
[20] Shirakawa, R., Yamashita, Y., Koda, D., Tsukizaki, R., Shimizu, Y., Tagawa, M., and Nishiyama, K., "Investigation and Experimental Simulation of Performance Deterioration of Microwave Discharge Ion Thruster M10 during Space Operation," *Acta Astronautica*, Vol. 174, 2020, pp. 367–376. https://doi.org/10.1016/j.actaastro.2020.05.004
[21] Yamashita, Y., Tsukizaki, R., Daiki, K., Tani, Y., Shirakawa, R., Hattori, K., and Nishiyama, K., "Plasma Hysteresis Caused by High-Voltage Breakdown in Gridded Microwave Discharge Ion Thruster M10," *Acta Astronautica*, Vol. 185, 2021, pp. 179–187. https://doi.org/10.1016/j.actaastro.2021.05.001
[22] Fu, S. H., and Ding, Z. F., "Characteristics of Microwave ECR Ion Thruster Powered with Plate Antenna in Cross-Magnetic Field: Standing Wave, Skin Effect, and Mode Transition," *Physics of Plasmas*, Vol. 28, No. 3, 2021, p. 033510. https://doi.org/10.1063/5.0033067
[23] Li, J.-Q. (李建泉), Xie, X.-Y. (谢新尧), Zhang, Q.-H. (张清和), Li, S.-H. (李书翰), and Lu, W.-Q. (陆文琪), "Data Processing of Langmuir Probe I–V Traces to Obtain Accurate Electron Temperature and Density in Maxwellian Plasmas," *Physics of Fluids*, Vol. 34, No. 6, 2022, p. 067115. https://doi.org/10.1063/5.0097089
[24] Farnell, C., "Numerical Simulation of HiPEP Ion Optics," *40th AIAA/ASME/SAE/ASEE Joint Propulsion Conference and Exhibit*, American Institute of Aeronautics and Astronautics, 2004. https://doi.org/10.2514/6.2004-3818
[25] Anderson, J., Katz, I., and Goebel, D., "Numerical Simulation of Two-Grid Ion Optics Using a 3D Code," *40th AIAA/ASME/SAE/ASEE Joint Propulsion Conference and Exhibit*, American Institute of Aeronautics and Astronautics, 2004. https://doi.org/10.2514/6.2004-3782
[26] Langmuir, I., and Blodgett, K. B., "Currents Limited by Space Charge between Concentric Spheres," *Physical Review*, Vol. 24, No. 1, 1924, pp. 49–59. https://doi.org/10.1103/PhysRev.24.49
[27] Zaim, H., and Alton, G. D., "Computational Design Studies for an Ion Extraction System for a 'Volume-Type' ECR Ion Source," *Review of Scientific Instruments*, Vol. 73, No. 2, 2002, pp. 595–597. https://doi.org/10.1063/1.1430511
[28] Bohm, D., "The Characteristics of Electrical Discharges in Magnetic Fields," McGraw-Hill, 1949.
[29] Goebel, D. M., and Katz, I., "Fundamentals of Electric Propulsion: Ion and Hall Thrusters," Wiley, 2008.
[30] Abgaryan, V. K., Akhmetzhanov, R. V., Loeb, H. W., Obukhov, V. A., and Cherkasova, M. V., "Numerical Simulation of a High-Perveance Ion-Extraction System with a Plasma Emitter," *Journal of Surface Investigation. X-ray, Synchrotron and Neutron Techniques*, Vol. 7, No. 6, 2013, pp. 1092–1099. https://doi.org/10.1134/S1027451013060037
[31] Li, H., and Sun, A., "Issues in the Numerical Modelling of Positive Ion Extraction," *Computer Physics Communications*, Vol. 259, 2021, p. 107629. https://doi.org/10.1016/j.cpc.2020.107629